

Forecasts on the contamination induced by unresolved point sources in primordial non-Gaussianity beyond Planck

A. Curto^{1,2} * M. Tucci^{3,4} J. González-Nuevo¹ L. Toffolatti⁵ E. Martínez-González¹
 F. Argüeso⁶ A. Lapi^{7,8} and M. López-Caniego¹

¹*Instituto de Física de Cantabria, CSIC-Universidad de Cantabria, Avda. de los Castros s/n, 39005 Santander, Spain*

²*Astrophysics Group, Cavendish Laboratory, Madingley Road, Cambridge CB3 0H3, U.K.*

³*LAL, Univ Paris-Sud, CNRS/IN2P3, Orsay, France*

⁴*Département de Physique Théorique and Center for Astroparticle Physics, Université de Genève, 24 quai Ansermet, CH-1211 Genève 4, Switzerland*

⁵*Departamento de Física, Universidad de Oviedo, c/ Calvo Sotelo s/n, 33007 Oviedo, Spain*

⁶*Departamento de Matemáticas, Universidad de Oviedo, c/ Calvo Sotelo s/n, 33007 Oviedo, Spain*

⁷*Dipartimento Fisica, Università Tor Vergata, Via Ricerca Scientifica 1, 00133 Roma, Italy*

⁸*Astrophysics Sector, SISSA, Via Bonomea 265, 34136 Trieste, Italy*

Accepted Received ; in original form

ABSTRACT

In this paper we present forecasts of the contamination on different shapes of the primordial non-Gaussianity f_{nl} parameter – detectable on future Cosmic Microwave Background (CMB) high-resolution anisotropy maps – produced by unresolved extragalactic point sources at frequencies of cosmological interest (45–375 GHz). We consider two scenarios: an ideal (noiseless) mission and a possible future space-borne satellite, with instrumental characteristics similar to the ones proposed for the Cosmic Origins Explorer (COre). The local, equilateral, orthogonal and flat shapes are considered in both temperature (intensity) and polarized emission data. The angular power spectrum and bispectrum of extragalactic point sources are estimated by state-of-the-art models of source number counts. The impact of all the most relevant (far-IR and radio selected) source populations on these shapes at COre frequencies is studied. The results of this analysis show that unresolved extragalactic point sources should not induce a very relevant non-Gaussian signal in the frequency range 100–200 GHz, thus not preventing a correct estimate of the CMB primordial f_{nl} parameter. Polarization information allows one to significantly reduce the error-bars in the f_{nl} parameter and the bias induced by unresolved sources and, hence, to widen the range of frequencies for f_{nl} studies. On the contrary, at $\nu < 100$ GHz or $\nu > 225$ GHz, important non-Gaussian deviations in CMB anisotropy maps are expected due to unresolved extragalactic sources.

Key words: methods: data analysis – cosmic microwave background – extragalactic points sources – radio and far-IR: galaxies

1 INTRODUCTION

The high precision achieved during the last years to detect possible weak non-Gaussian signals with primordial origin in the most precise CMB anisotropy data maps (such as WMAP¹ data, the forthcoming Planck² data and future missions) stresses the importance of the characterization of all the possible non-primordial contami-

nants. The standard models of inflation (Starobinskiĭ 1979; Guth 1981; Albrecht & Steinhardt 1982; Linde 1982, 1983; Mukhanov et al. 1992) predict that the primordial fluctuations, linearly imprinted in the CMB anisotropies, are nearly compatible with a Gaussian distribution. Any departure from Gaussianity with a primordial origin would challenge our understanding of the physics of the early Universe. From a practical point of view, the first approach to detect non-Gaussian deviations is the study of the third order moments (the so-called bispectrum) of the anisotropy map. For most of the cases with a physical interest, this bispectrum is usually characterised

* E-mail: curto@ifca.unican.es, acurto@mrao.cam.ac.uk

¹ <http://map.gsfc.nasa.gov/>

² <http://www.esa.int/planck>

by a single amplitude, the non-linear coupling parameter f_{nl} (see e.g. Verde et al. 2000; Komatsu & Spergel 2001; Bartolo et al. 2004; Babich et al. 2004; Babich 2005). For recent reviews of the status of the primordial non-Gaussianity characterization see e.g. Bartolo et al. (2010); Yadav & Wandelt (2010); Liguori et al. (2010); Martínez-González & Planck Collaboration (2012).

The best estimates of the f_{nl} parameter can currently be obtained using the publicly available WMAP data. Three different shapes with relevant interest for the physics of inflation have been constrained using these data: the local, equilateral and orthogonal f_{nl} shapes. Information about the inflationary scenarios that can produce these and other non-Gaussian shapes can be found for example in the reviews by Bartolo et al. (2004); Yadav & Wandelt (2010). The instrumental noise contamination and the beam size of the WMAP 61 and 94 GHz frequency channels allow a maximum resolution of $\ell_{max} \sim 1000$. The best estimates of these shapes provided by the WMAP collaboration (Komatsu et al. 2011) are $\hat{f}_{nl}^{loc} = 32 \pm 21$, $\hat{f}_{nl}^{eq} = 26 \pm 140$ and $\hat{f}_{nl}^{ort} = -202 \pm 104$ (68% CL) for the local, equilateral and the orthogonal shapes respectively (see e.g. Curto et al. 2011, 2012, for independent analyses with similar results).

Unresolved point sources introduce non-Gaussian fluctuations in CMB anisotropies at a detectable level. In the past, their “contamination” to the CMB angular bispectrum has been studied in detail by many authors (e.g. Refregier et al. 2000; Komatsu & Spergel 2001; Argüeso et al. 2003; González-Nuevo et al. 2005; Argüeso et al. 2006; Babich & Pierpaoli 2008; Serra & Cooray 2008). As an example, the contamination of the f_{nl} parameter due to point sources in WMAP data has been studied by Komatsu et al. (2009) considering the simple constant-flux model to simulate the radio sources. They found that the bias introduced in the local and the equilateral shapes is $\Delta f_{nl}^{(loc)} \sim 2$, $\Delta f_{nl}^{(eq)} \sim 22$. Taking into account the source number counts model by de Zotti et al. (2005), Curto et al. (2011) estimated that the bias in f_{nl} is $\Delta f_{nl}^{(loc)} \sim 2.5$, $\Delta f_{nl}^{(eq)} \sim 37$ and $\Delta f_{nl}^{(ort)} \sim 25$. More recently, by exploiting publicly available all-sky simulations, Lacasa et al. (2012) have tried to characterize the configuration dependence and the frequency behavior of the bispectra originated by “radio” and “far-infrared” extragalactic sources. Their results show that the bispectrum due to (extragalactic) far-infrared sources starts to dominate that of radio sources on large angular scales at 150 GHz and dominates on the whole multipole range at 350 GHz.

In this paper we characterize the contamination that unresolved extragalactic point sources introduce in the CMB bispectrum by using the best available predictions on number counts of “radio” sources, i.e. Active Galactic Nuclei (AGN) with emission spectra dominated by synchrotron radiation (in this frequency range), and of “far-infrared” (far-IR) sources, i.e. low- and high-redshift galaxies in which the microwave emission is dominated by warm/cold dust in thermal equilibrium with the radiation field. We also discuss the effect of unresolved *polarized* extragalactic sources in “future” CMB anisotropy experiments. In particular, we make specific predictions for different frequency channels foreseen for the future Cosmic Origin Explorer (CORE) satellite mis-

sion (The CORE Collaboration et al. 2011), which has been recently submitted to the European Space Agency (ESA) Horizon 2015-2025 Programme.³

Our current predictions of number counts of extragalactic sources are based on two different models: the first one, by Tucci et al. (2011), is able to give the most precise predictions on high-frequency ($\nu \geq 100$ GHz) number counts of radio sources using physically motivated recipes to describe the complex spectral behavior of blazars, that dominate the mm-wave counts at bright flux densities; the second one, by Lapi et al. (2011), using a simple physical model and a single reference Spectral Energy Distribution (SED), has proved able to reproduce very well all the most recent measures (by Herschel, BLAST, etc.) of number counts of extragalactic sources at sub-mm wavelengths. It is important to mention that, to our knowledge, this is the first time that predictions on the impact of extragalactic radio and far-IR/sub-mm sources on the CMB angular power spectrum, bispectrum and other statistics are performed with the level of detail discussed here.

In Section 2 we describe the extragalactic point source population in this frequency range. The models that characterise their power spectrum are presented in Section 3. Section 4 reviews the basic formalism for the angular bispectrum and the four bispectrum shapes. Section 5 introduces the point source bispectra and the estimator to measure the Δf_{nl} bias. The forecasts for the CORE mission are given in Section 6 and, finally, in Section 7 the conclusions are listed.

2 EXTRAGALACTIC POINT SOURCES

In this section we describe the expected contribution of extragalactic point sources to temperature and polarization fluctuations from centimetre to sub-millimetre wavelengths. In this range of frequencies, extragalactic sources are typically divided in two populations, according to the physical radiative mechanism involved: far-infrared (far-IR) sources dominated by thermal dust emission and radio sources dominated by synchrotron emission. In the following analysis we use number counts predictions obtained by two very recent models: i.e., Tucci et al. (2011, T11, hereafter), as for radio sources at cm to mm wavelengths and Lapi et al. (2011, L11, hereafter), as for far-IR/submm sources. In both cases, these models provide predictions on source number counts and related statistics which have shown a very good agreement with observational data.

³ The CORE mission has not been selected by ESA in the 2011 first call for proposals. However, a CORE-like space mission with technical characteristics similar to the present ones could be hopefully funded in the near future, given that its very high scientific output has been already acknowledged by the ESA Space Science Advisory Committee (SSAC). In fact, a CORE-like mission will be of fundamental scientific importance for detecting the imprint left by primordial gravitational waves on polarized CMB anisotropies, since the amplitude of primordial gravitational waves is directly proportional to the energy scale at which the inflation occurred. We don’t know the exact instrumental characteristics of this future space mission. However, we do useful predictions by using the current instrumental technical details quoted in the proposal (The CORE Collaboration et al. 2011).

2.1 Radiosources

Recent evolutionary models for Extragalactic Radio Sources (ERS) by de Zotti et al. (2005) and Massardi et al. (2010) are capable of providing a good fit to number counts from ~ 100 MHz and up to ~ 100 GHz. They adopt a simple power-law, i.e. $S(\nu) \propto \nu^\alpha$, with an almost flat spectral index ($\alpha \simeq -0.1$) for extrapolating spectra of blazar sources⁴ at high frequencies. These models, however, over-predict the number counts of extragalactic synchrotron sources detected by the Atacama Cosmology Telescope (ACT) at 148 GHz (Marriage et al. 2011) and by Planck in all the High Frequency Instrument (HFI) channels (Planck Collaboration XIII 2011; Planck Collaboration VII 2013). The main reason for this disagreement is the spectral steepening observed in Planck Early Release Compact Source Catalogue (ERCSC) sources at above ~ 70 GHz (Planck Collaboration VII 2011; Planck Collaboration XV 2011) and already suggested by other data sets (González-Nuevo et al. 2008; Sadler et al. 2008).

The more recent models by T11 use physically grounded recipes to describe the complex spectral behaviour of blazars, which dominate the mm-wavelengths number counts at bright flux densities. The main novelty of these models is the statistical prediction of a break frequency, ν_M , in spectra of blazars in agreement with classical physical models for the synchrotron emission produced in blazar jets (e.g., Blandford & Königl 1979). The most successful of these models is referred to as C2Ex⁵. This model is able to give a very good fit to all the data of bright extragalactic radio sources available so far: number counts up to ~ 500 – 600 GHz and on spectral index distributions up to, at least, 200–300 GHz (see T11 and Planck Collaboration VII 2013; López-Caniego et al. 2012).

Polarization in ERS is typically observed to be a few percent of total intensity at cm or mm wavelengths (e.g., Murphy et al. 2010; Battye et al. 2011; Sajina et al. 2011), with only very few objects showing a fractional polarization, $\Pi = P/S$, as high as $\sim 10\%$. We refer to the recent paper by Tucci & Toffolatti (2012) in order to characterize polarization properties of ERS and their contribution to power spectra. In that work authors show that the distribution of the fractional polarization for blazars is well described by a log-normal distribution with values of the median fractional polarization, Π_{med} , and of $\langle \Pi^2 \rangle^{1/2}$ depending on the frequency. At frequencies $\nu \gtrsim 40$ GHz we take $\Pi_{med} = 0.04, 0.03, 0.036$ and $\langle \Pi^2 \rangle^{1/2} = 0.06, 0.038, 0.045$ for steep-spectrum sources, FSRQs and BL Lacs, respectively. These values are intermediate between the two "extreme" cases discussed in Tucci & Toffolatti (2012) and rely on the most recent data at 86 GHz of Agudo et al. (2010).

⁴ Blazars are jet-dominated extragalactic objects, observed within a small angle of the jet axis and characterized by a highly variable non-thermal synchrotron emission at GHz frequencies, in which the beamed component dominates the observed emission (Angel & Stockman 1980)

⁵ It assumes different distributions of break frequencies for BL Lac objects and Flat Spectrum Radio Quasars (FSRQs) – with the relevant synchrotron emission coming from more compact regions in jets of the former objects. See T11 for more details.

2.2 Far-IR Sources

Recent data acquired by The Herschel Astrophysical Terahertz Large Area Survey (H-ATLAS Eales et al. 2010), the largest area survey carried out by the Herschel Space Observatory (Pilbratt et al. 2010), have demonstrated that far-IR sources comprise both a low- z galaxy population, identified through matching to the Sloan Digital Sky Survey (York et al. 2000) data (Smith et al. 2011), and a high- z population (median redshift ~ 2) identified through their far-IR colors (Amblard et al. 2010). Low- z galaxies are generally normal/star-forming late-type galaxies with moderate opacity (Dunne et al. 2011; Smith et al. 2012). Through analyses of clustering these two populations are found to be very different; the low- z population ($z < 0.3$) does cluster like star-forming blue galaxies (Maddox et al. 2010; Guo et al. 2011; van Kampen et al. 2012), whereas the high- z population clusters much more strongly, suggesting that the high- z sources reside in more massive halos (Maddox et al. 2010).

In the case of late-type infrared galaxies, we adopt the same source number counts as in L11, previously derived by Negrello et al. (2007). As explained in more detail in that paper, the contributions of the this type of galaxies to the number counts were estimated following a phenomenological approach, which consists of simple analytic recipes to evolve backwards their local LFs with cosmic time, as well as of appropriate templates for their SEDs, to compute K-corrections.

Regarding star-forming proto-spheroidal galaxies, the 100 and 250 μm luminosity functions (LF) at different redshifts are quite well reproduced by the physical model of Early Type Galaxy (ETG) formation and evolution by Granato et al. (2001, 2004), further elaborated by Lapi et al. (2006), and recently revised by L11 without any adjustment of the parameters. As discussed in these papers, the model is built in the framework of the standard hierarchical clustering scenario. This model was the basis for the successful predictions of the submillimetre counts of strongly lensed galaxies by Negrello et al. (2007). It also accurately reproduced the epoch-dependent galaxy LFs in different spectral bands, as well as a variety of relationships among photometric, dynamical, and chemical properties, as shown in previous papers (see Table 2 of Lapi et al. 2006) and additional results, especially on the galaxy chemical evolution, in Mao et al. (2007); Lapi et al. (2008).

Number counts from the L11 model are observed to be slightly high at mm wavelengths⁶. The model, in fact, tends to overestimate the Poisson contribution to the power spectrum of intensity fluctuations measured at frequencies ≤ 353 GHz by *Planck* (Planck Collaboration XVIII 2011), SPT (Hall et al. 2010) and ACT (Dunkley et al. 2011). Scaling down counts by constant factors is however enough to comply with measurements at mm wavelengths (Xia et al. 2012). In this work we multiply number counts by the following factors: 0.81 and 0.71 at 375 and 225 GHz, 0.55 for $\nu \leq 165$ GHz.

Finally, as predicted by Blain (1996); Perrotta et al.

⁶ This effect is due to the fact that the SED of high redshift objects (that contribute to the mm counts around 10–30 mJy) are slightly different to the template adopted in L11 as a universal SED for protospheroids.

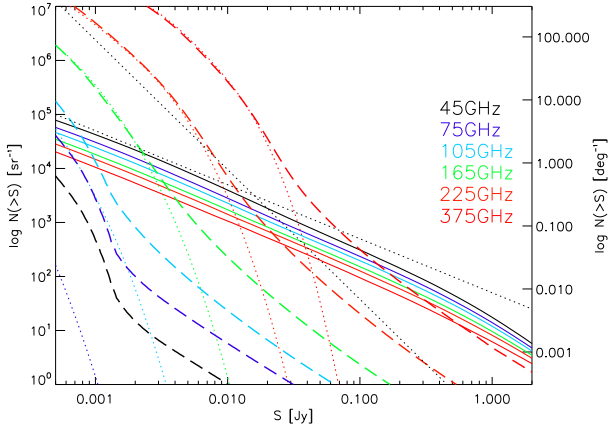


Figure 1. Predicted integral number counts of radio sources (solid lines; T11 model) and of far-IR sources (total counts: dashed lines; proto-spheroidal galaxies only: dotted lines; L11 model) at the frequencies indicated inside the panel (each frequency and the corresponding curves are displayed by a different colour). The two black dotted lines, plotted as a reference, represent two power laws, with slopes 1 and 3, respectively.

(2002, 2003); Negrello et al. (2007); Paciga et al. (2009); Lima et al. (2010) among others, the combination of the very steep number counts in the far-IR/sub-mm and of high redshifts – hence large lensing optical depths – maximizes the fraction of strongly lensed sources. In the case of the L11 model, the contribution from lensed proto-spheroidal galaxies were estimated using the amplification distribution of Perrotta et al. (2003); Negrello et al. (2007); Lapi et al. (2012). Such predictions were recently confirmed by Negrello et al. (2010); González-Nuevo et al. (2012) by using the Science Demonstration Phase data of the H-ATLAS survey. For the current work we have considered that the strong gravitational lensing effect is a random process, and therefore, the lensed proto-spheroidal galaxies show a Poisson spatial distribution. Due to their lack of correlation with the un-lensed proto-spheroidal galaxy sky distribution, we have treated them as a different population.

Regarding polarization, all the - very few - data so far collected on the polarization of far-IR/sub-mm sources (dusty early- or late-type galaxies and Galactic dust clouds) do indicate that the total polarized emission of these sources has to be very low with median values at around 1-2% level. Moreover, in many observations, no polarized emission (or compatible with zero) has been detected (Dotson et al. 2010; Vaillancourt 2011). Due to the above, we have assumed – for the population of far-IR selected sources as a whole – a (conservative) average polarization level of 1%.

3 CONTAMINATION OF POINT SOURCES TO CMB POWER SPECTRA

In Fig. 1 we directly compare expected integrated number counts of radio and far-IR sources from the T11 and L11 models at frequencies ranging from 45 to 375 GHz – i.e. the frequencies interesting for CMB studies. The figure well emphasizes the different behavior of the two populations in terms of flux density distribution and frequency spectrum.

In the case of ERS, we can notice that the slope of integral counts ($N(> S) \propto S^{-\beta}$) is not very different from $\beta \simeq 1$ at $S < 1$ Jy. This means that the contamination of unresolved ERS to the CMB power spectra is almost proportional to the flux density limit, S_c , above which sources can be detected and removed or masked. Moreover, because the spectra of blazars are typically flat or moderately steep, $-1 \lesssim \alpha \lesssim 0$, integral counts change slowly with the frequency, decreasing by only a factor 2–4 from 44 to 350 GHz, depending on the flux density considered.

On the other hand, far-IR source counts increase very steeply when moving to low flux densities, due to the contribution of proto-spheroidal galaxies (see dotted lines in Fig. 1). The general slope of far-IR integral counts, β , is between 2 and 3 depending on the flux density range. As a consequence, the amplitude of power spectra for unresolved far-IR sources is almost insensitive to the value of S_c , at least for flux density limits typically obtained in large-area CMB experiments. Finally, because of the steep frequency spectrum of dust emission, $N(> S)$ is also strongly dependent on frequency, making the contribution of far-IR sources already completely negligible at frequencies $\nu \gtrsim 100$ GHz (see Fig. 2).

In terms of power spectra, it is well known that point sources without spatial correlations have:

$$C_\ell^{white} = k_\nu^2 \int_0^{S_c} S^2 \frac{dn}{dS} dS \quad (1)$$

where $k_\nu^{-1} = dB_0/dT_0$ is the conversion factor from flux density to temperature units (see e.g. Tegmark & Efstathiou 1996), S_c is the flux density limit for the unresolved point sources and dn/dS is number counts that characterise the population of sources. However, powerful high- z far-IR sources have been shown to be highly correlated by, e.g., recent measures from *Herschel* (Amblard et al. 2011; Viero et al. 2012) and *Planck* (Planck Collaboration XVIII 2011). For the other extragalactic source populations the clustering is negligible (Toffolatti et al. 2005; Negrello et al. 2007). Therefore, we shall consider the contribution of clustered sources to angular power spectra (and bispectra) only for dusty proto-spheroidal galaxies. This is estimated from realistic simulations of two-dimensional distributions of clustered point sources (see González-Nuevo et al. 2005). This software was also implemented in the Planck Sky Model (Delabrouille et al. 2012) and its predictions on the power spectrum of cosmic infrared background anisotropies have been shown to be in good agreement with the latest Planck measurements (Planck Collaboration XVIII 2011).

The total power spectra from point sources are then given by the sum of the following components:

$$C_\ell^{ps} = C_\ell^{rad,white} + C_\ell^{ir,white} + C_\ell^{sph,clust} \quad (2)$$

where $C_\ell^{rad,white}$ and $C_\ell^{ir,white}$ are the constant term from shot-noise power spectra of radio and far-IR (which includes late-type, lensed and proto-spheroidal galaxies) sources, and $C_\ell^{sph,clust}$ is the power spectrum from the clustered contribution of proto-spheroidal galaxies⁷.

⁷ We remind the reader that the total power spectrum of a population of clustered sources is $C_\ell^{tot} = C_\ell^{white} + C_\ell^{clust}$.

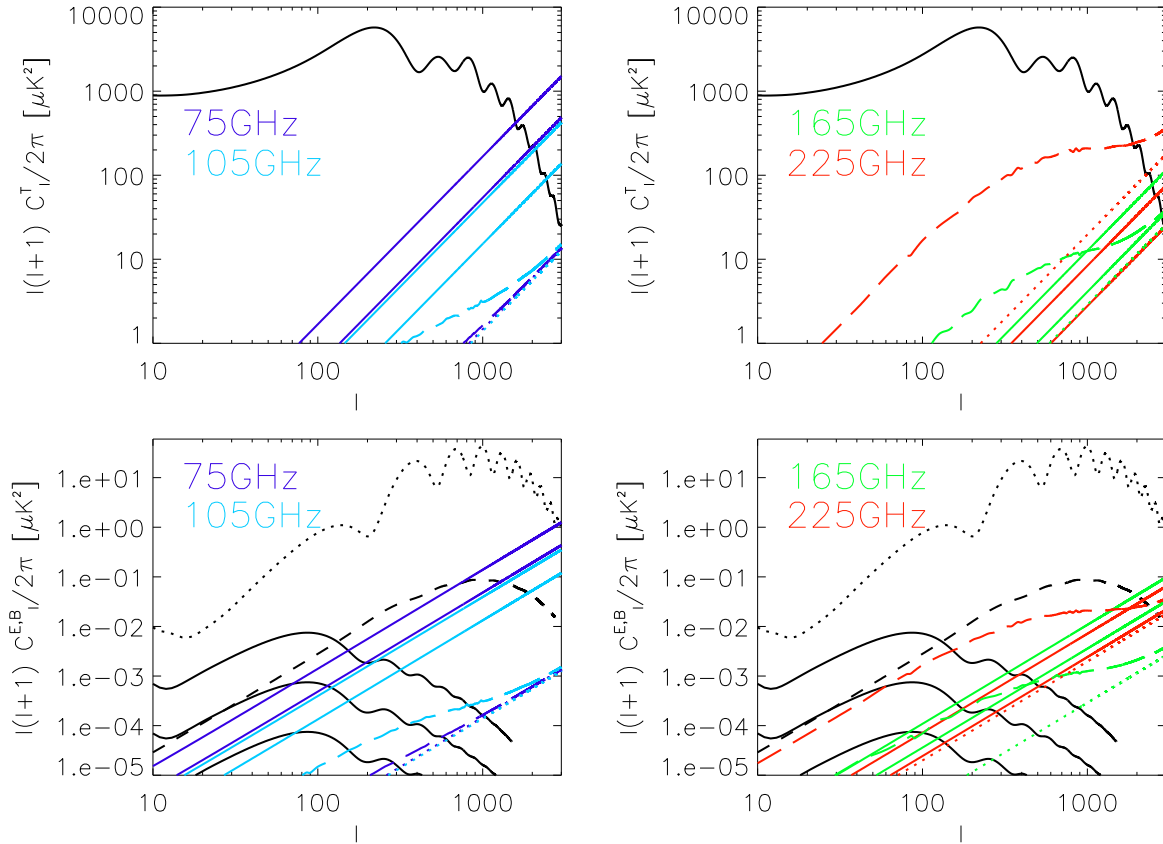


Figure 2. Point source power spectra for temperature (top panels) and polarization (bottom panels) at 75, 105, 165 and 225 GHz. Lines in colour are for radio sources (solid lines) and for far-IR sources (dashed lines for the total contribution; dotted lines for the Poisson contribution). We consider two flux density limits for radio sources: $S_c = 1$ and 0.3 Jy; for far-IR sources we plot only the case with $S_c = 1$ (there are not significant differences taking $S_c = 0.3$). Black lines are for CMB spectra from the fiducial WMAP 7-year model: in the *bottom panels* dotted lines are for the E-mode, dashed lines for lensing-induced B-mode and solid lines for primordial B-mode with $r = 0.1, 0.01, 10^{-3}$.

Regarding polarization, point sources contribute, on average, equally to power spectra of E- and B-modes or equivalently to Q and U power spectra in the flat-sky limit. Polarization power spectra of point sources are proportional to the temperature power spectrum (Tucci et al. 2004): for the Q power spectrum, e.g., we have

$$C_\ell^Q = k_\nu^2 \langle S^2 p^2 \cos^2(2\phi) \rangle = \frac{k_\nu^2}{2} \langle p^2 \rangle C_\ell^T. \quad (3)$$

The above relation assumes that the flux density S , the polarization fraction p and the polarization angle in the chosen reference system ϕ are independent variables (see Tucci & Toffolatti 2012, for a detailed discussion on this assumption). On the other hand, all the cross-power spectra are equal to zero:

$$\begin{aligned} C_\ell^{TQ} &\propto \langle S^2 p \cos(2\phi) \rangle = 0 \\ C_\ell^{TU} &\propto \langle S^2 p \sin(2\phi) \rangle = 0 \\ C_\ell^{QU} &\propto \langle S^2 p^2 \cos(2\phi) \sin(2\phi) \rangle = 0. \end{aligned} \quad (4)$$

Fig. 2 shows model predictions for temperature and polarization power spectra at 75, 105, 165 and 225 GHz. We also consider two possible flux density limits, i.e. $S_c = 1$ and 0.3 Jy.

As previously discussed, far-IR spectra are almost insensitive to the choice of S_c , especially for the clustered contribution. Comparing the two source populations, we see that radio sources are dominant at $\nu \lesssim 100$ GHz, while far-IR sources start to dominate at $\nu \gtrsim 200$ GHz both in temperature and polarization. At intermediate frequencies, i.e. $100 < \nu < 200$ GHz, ERS are the main contaminant at high multipoles ($\ell > 1000$), but not for $\ell \lesssim 1000$, where the far-IR clustered sources contribution becomes higher than the ERS power spectrum in temperature and comparable in polarization.

Because proto-spheroidal galaxies are the only clustered population in the L11 model, it is worth discussing more in detail their relevance in terms of power spectrum. In Fig. 3 we plot the ratio of the total spectrum of proto-spheroidal galaxies to their shot-noise spectrum, $C_\ell^{\text{sph}}/C_\ell^{\text{sph,white}}$, and to the shot-noise spectrum of all far-IR sources, $C_\ell^{\text{sph}}/C_\ell^{\text{ir,white}}$, (the former ratio enters later in Eq. 18 and gives us the increase of the bispectrum due to clustering). As the frequency decreases, we observe two effects: *a*) the contribution of proto-spheroidal galaxies to the far-IR power spectrum becomes less and less important; *b*) moreover, the relative contribution of clustering to proto-spheroidal power spectrum reduces. The reason of

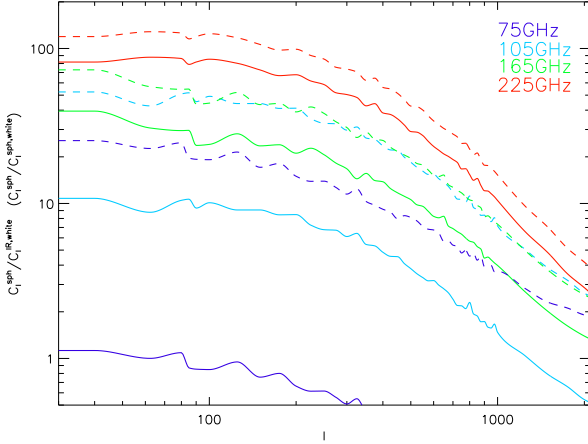


Figure 3. The ratio of the total spectrum, C_ℓ^{sph} , to the shot-noise spectrum, $C_\ell^{sph,white}$, of proto-spheroidal galaxies (dashed lines), and to the shot-noise spectrum from far-IR sources, $C_\ell^{ir,white}$ (solid lines), at the frequencies indicated in the panel.

these trends is related to the shift of the redshift distribution of submillimetre bright galaxies to higher redshift with increasing the wavelength, as effect of the strongly negative K -correction (L11). At high z , however, massive proto-spheroidal galaxies become increasingly rare and the slope of number counts at low frequencies is not as steep as that at sub-mm wavelengths. As a consequence, the shot-noise term of the power spectrum, dominated by bright sources, has more weight with respect to the clustered one (dominated by faint sources).

Finally, we discuss the contamination of extragalactic sources to CMB fluctuations: in the frequency range considered, it is relevant only at very high ℓ ($\gtrsim 2000$) for temperature and is essentially negligible for the E-mode polarization (see Fig. 2). This is not the case for the B-mode polarization arisen from primordial gravitational waves if $r < 0.01$. A subtraction of point sources at levels even lower than ones shown in Fig. 2 is not an easy task. For radio sources, this could be in principle done *a*) by removing/masking sources down to flux density limits of $S < 0.3$ Jy or *b*) by a direct measurement of the power spectrum of polarization fluctuations at small angular scales. In both cases observations with arcmin resolution are required. Far-IR sources are still more challenging to deal with, and the previous methods are not valid to clean their contamination due to the high correlated signal. Instead, approaches similar to ones used for diffuse Galactic foregrounds should be more suitable for this goal, although they are model dependent.

4 THE ANGULAR BISPECTRUM

The CMB angular bispectrum is defined in terms of cubic combinations of the spherical harmonic coefficients of the CMB anisotropies of the T, E and B modes:

$$B_{\ell_1 \ell_2 \ell_3, m_1 m_2 m_3}^{ijk} \equiv \langle a_{\ell_1 m_1}^i a_{\ell_2 m_2}^j a_{\ell_3 m_3}^k \rangle, \quad (5)$$

where the indices $\{i, j, k\}$ cover the T, E and B modes. The angular-averaged bispectrum and the reduced angular-

averaged bispectrum, $B_{\ell_1 \ell_2 \ell_3}^{ijk}$ and $b_{\ell_1 \ell_2 \ell_3}^{ijk}$ are defined as:

$$B_{\ell_1 \ell_2 \ell_3}^{ijk} = \sum_{m_1 m_2 m_3} \begin{pmatrix} \ell_1 & \ell_2 & \ell_3 \\ m_1 & m_2 & m_3 \end{pmatrix} B_{\ell_1 \ell_2 \ell_3, m_1 m_2 m_3}^{ijk} = b_{\ell_1 \ell_2 \ell_3}^{ijk} \begin{pmatrix} \ell_1 & \ell_2 & \ell_3 \\ 0 & 0 & 0 \end{pmatrix} \sqrt{\frac{(2\ell_1+1)(2\ell_2+1)(2\ell_3+1)}{4\pi}}. \quad (6)$$

The reduced bispectrum can be written as (see, e.g. Yadav & Wandelt 2010):

$$b_{\ell_1 \ell_2 \ell_3}^{ijk} = (4\pi)^3 (-i)^{\ell_1 + \ell_2 + \ell_3} \sum_{m_1 m_2 m_3} \begin{pmatrix} \ell_1 & \ell_2 & \ell_3 \\ m_1 & m_2 & m_3 \end{pmatrix} \times \int \frac{d^3 k_1}{(2\pi)^3} \frac{d^3 k_2}{(2\pi)^3} \frac{d^3 k_3}{(2\pi)^3} Y_{\ell_1 m_1}^*(\hat{k}_1) Y_{\ell_2 m_2}^*(\hat{k}_2) Y_{\ell_3 m_3}^*(\hat{k}_3) g_{\ell_1}^i(k_1) g_{\ell_2}^j(k_2) g_{\ell_3}^k(k_3) \langle \Phi(\mathbf{k}_1) \Phi(\mathbf{k}_2) \Phi(\mathbf{k}_3) \rangle, \quad (7)$$

where $g_\ell^i(k)$ is the transfer function for temperature or polarization⁸ and $\langle \Phi(\mathbf{k}_1) \Phi(\mathbf{k}_2) \Phi(\mathbf{k}_3) \rangle$ is the 3-point correlation function in Fourier space of the Bardeen's curvature perturbations $\Phi(\mathbf{x})$. The 3-point correlation function can be given in terms of the so-called shape function $F(k_1, k_2, k_3)$:

$$\langle \Phi(\mathbf{k}_1) \Phi(\mathbf{k}_2) \Phi(\mathbf{k}_3) \rangle = (2\pi)^3 \delta^3(\mathbf{k}_1 + \mathbf{k}_2 + \mathbf{k}_3) F(k_1, k_2, k_3) \quad (8)$$

The level of primordial non-Gaussianity is parametrised by the non-linear coupling parameter f_{nl} (Verde et al. 2000; Komatsu & Spergel 2001; Bartolo et al. 2004; Yadav & Wandelt 2010). This parameter measures departures from zero of the bispectrum. Depending on the physical mechanisms of the different inflationary models the shape function can take different forms. The shapes that we consider in this work are the local, equilateral, orthogonal and flat shapes.

- **Local shape.** This type of Non-Gaussianity is generated in multi-field inflationary models (Komatsu et al. 2005; Komatsu 2010), the curvaton (Lyth et al. 2003), the inhomogeneous reheating scenario (Dvali et al. 2004; Bartolo et al. 2004), hybrid inflation (Lin 2009), etc. Its shape is given by (see e.g. Creminelli et al. 2006; Yadav & Wandelt 2010):

$$F(k_1, k_2, k_3) = 2A^2 f_{nl} \left[\frac{1}{k_1^{3-(n_s-1)} k_2^{3-(n_s-1)}} + (2 \text{ perm}) \right], \quad (9)$$

where A is the amplitude of the power spectrum and n_s is the spectral index (Komatsu et al. 2011). Most of the signal of this type of bispectrum is located in squeezed configurations such as $k_1 \simeq k_2 \gg k_3$ (Creminelli et al. 2006; Yadav & Wandelt 2010; Martínez-González & Planck Collaboration 2012).

- **Equilateral shape.** This type of Non-Gaussianity is generated in the Dirac-Born-Infeld inflation (Silverstein & Tong 2004; Bartolo et al. 2004; Langlois et al. 2008), ghost inflation (Arkani-Hamed et al. 2004), single-field inflationary models in Einstein gravity

⁸ This function can be computed numerically using the CAMB (Lewis et al. 2000) software <http://camb.info>

(Chen et al. 2007) etc. Its shape is given by (see e.g. Creminelli et al. 2006; Yadav & Wandelt 2010):

$$F(k_1, k_2, k_3) = 6A^2 f_{nl} \left[-\frac{1}{k_1^{3-(n_s-1)} k_2^{3-(n_s-1)}} + (2 \text{ perm}) \right. \\ \left. - \frac{2}{(k_1 k_2 k_3)^{2(4-n_s)/3}} \right. \\ \left. + \left\{ \frac{1}{k_1^{(4-n_s)/3} k_2^{2(4-n_s)/3} k_3^{(4-n_s)}} + (5 \text{ perm}) \right\} \right]. \quad (10)$$

Most of the signal of this type of bispectrum is located in equilateral configurations such as $k_1 \simeq k_2 \simeq k_3$ (see e.g. Creminelli et al. 2006; Yadav & Wandelt 2010; Martínez-González & Planck Collaboration 2012).

• **Orthogonal shape.** This type of Non-Gaussianity is generated in general single-field models (Cheung et al. 2008; Senatore et al. 2010). Its shape is given by (see e.g. Senatore et al. 2010; Yadav & Wandelt 2010; Komatsu et al. 2011):

$$F(k_1, k_2, k_3) = 6A^2 f_{nl} \left[-\frac{3}{k_1^{3-(n_s-1)} k_2^{3-(n_s-1)}} + (2 \text{ perm}) \right. \\ \left. - \frac{8}{(k_1 k_2 k_3)^{2(4-n_s)/3}} \right. \\ \left. + \left\{ \frac{3}{k_1^{(4-n_s)/3} k_2^{2(4-n_s)/3} k_3^{(4-n_s)}} + (5 \text{ perm}) \right\} \right]. \quad (11)$$

This bispectrum peaks in both equilateral $k_1 \simeq k_2 \simeq k_3$ and flat-triangle configurations such as $k_1 = k_2 + k_3$ (see the shape figures e.g. in Senatore et al. 2010; Martínez-González & Planck Collaboration 2012).

• **Flat shape.** This type of Non-Gaussianity is generated for example in models with modifications in the initial state of the inflaton field (see e.g. Meerburg et al. 2009, and references therein), single-field models with high derivative iterations (Bartolo et al. 2010b) among others. Its shape is given by (Meerburg et al. 2009):

$$F(k_1, k_2, k_3) = 6A^2 f_{nl} \left[\frac{1}{k_1^{3-(n_s-1)} k_2^{3-(n_s-1)}} + (2 \text{ perm}) \right. \\ \left. + \frac{3}{(k_1 k_2 k_3)^{2(4-n_s)}} \right. \\ \left. - \left\{ \frac{1}{k_1^{(4-n_s)/3} k_2^{2(4-n_s)/3} k_3^{(4-n_s)}} + (5 \text{ perm}) \right\} \right]. \quad (12)$$

This bispectrum peaks in flat-triangle configurations $k_1 = k_2 + k_3$ (see the shape figure in Meerburg et al. 2009).

Using the shape forms defined in Eqs. 9, 10, 11, 12 and the CMB bispectrum in Eq. 7 we have:

$$(b_{\ell_1 \ell_2 \ell_3}^{loc})^{ijk} = 2 \int_0^\infty x^2 dx \left[\alpha_{\ell_1}^i(x) \beta_{\ell_2}^j(x) \beta_{\ell_3}^k(x) + (2 \text{ perm}) \right], \quad (13)$$

$$(b_{\ell_1 \ell_2 \ell_3}^{eq})^{ijk} = 6 \int_0^\infty dx x^2 \left[-\alpha_{\ell_1}^i(x) \beta_{\ell_2}^j(x) \beta_{\ell_3}^k(x) + (2 \text{ perm}) \right. \\ \left. + \beta_{\ell_1}^i(x) \gamma_{\ell_2}^j(x) \delta_{\ell_3}^k(x) + (5 \text{ perm}) - 2\delta_{\ell_1}^i(x) \delta_{\ell_2}^j(x) \delta_{\ell_3}^k(x) \right], \quad (14)$$

$$(b_{\ell_1 \ell_2 \ell_3}^{ort})^{ijk} = 18 \int_0^\infty dx x^2 \left[-\alpha_{\ell_1}^i(x) \beta_{\ell_2}^j(x) \beta_{\ell_3}^k(x) + (2 \text{ perm}) \right. \\ \left. + \beta_{\ell_1}^i(x) \gamma_{\ell_2}^j(x) \delta_{\ell_3}^k(x) + (5 \text{ perm}) - \frac{8}{3} \delta_{\ell_1}^i(x) \delta_{\ell_2}^j(x) \delta_{\ell_3}^k(x) \right] \quad (15)$$

and

$$(b_{\ell_1 \ell_2 \ell_3}^{flat})^{ijk} = 6 \int_0^\infty dx x^2 \left[\alpha_{\ell_1}^i(x) \beta_{\ell_2}^j(x) \beta_{\ell_3}^k(x) + (2 \text{ perm}) \right. \\ \left. - \beta_{\ell_1}^i(x) \gamma_{\ell_2}^j(x) \delta_{\ell_3}^k(x) + (5 \text{ perm}) + 3\delta_{\ell_1}^i(x) \delta_{\ell_2}^j(x) \delta_{\ell_3}^k(x) \right] \quad (16)$$

where $\alpha_\ell^i(x)$, $\beta_\ell^i(x)$, $\gamma_\ell^i(x)$, $\delta_\ell^i(x)$ are filter functions defined in terms of the power spectrum $P(k)$ and the transfer functions $g_\ell^i(k)$ (see e.g. Fergusson et al. 2010a,b; Yadav & Wandelt 2010; Curto et al. 2011, for their actual definitions).

5 BIAS AND UNCERTAINTIES ON PRIMORDIAL NON-GAUSSIANITY

5.1 Bispectrum of point sources

The bispectrum of a point source population without spatial correlations, as the case of radio sources, is well characterised and is constant with ℓ :

$$b_{\ell_1 \ell_2 \ell_3}^{white} = k_\nu^3 \int_0^{S_c} S^3 \frac{dn}{dS} dS. \quad (17)$$

On the other hand, far-IR sources have spatial correlations. According to the widely used prescription by Argüeso et al. (2003), also considered e.g. in González-Nuevo et al. (2005); Argüeso et al. (2006) and extended to the full sky by Lacasa et al. (2012), the total bispectrum for a single clustered sources population can be written as:

$$b_{\ell_1 \ell_2 \ell_3}^{tot} \equiv b_{\ell_1 \ell_2 \ell_3}^{white} \sqrt{\frac{C_{\ell_1}^{tot} C_{\ell_2}^{tot} C_{\ell_3}^{tot}}{C_{\ell_1}^{white} C_{\ell_2}^{white} C_{\ell_3}^{white}}}. \quad (18)$$

The total bispectrum of point sources is then given by the sum of the shot-noise contributions of ERS ($b_{\ell_1 \ell_2 \ell_3}^{rad, white}$) and of far-IR late-type and lensed galaxies ($b_{\ell_1 \ell_2 \ell_3}^{lt+le, white}$) plus the ‘‘clustered’’ bispectrum of proto-spheroidal galaxies ($b_{\ell_1 \ell_2 \ell_3}^{sph}$) as given by Eq. 18:

$$b_{\ell_1 \ell_2 \ell_3}^{ps} = b_{\ell_1 \ell_2 \ell_3}^{rad, white} + b_{\ell_1 \ell_2 \ell_3}^{lt+le, white} + b_{\ell_1 \ell_2 \ell_3}^{sph}. \quad (19)$$

When polarization is considered, we have 10 different bispectra arisen from all the possible combinations of temperature and polarization E - and B -modes. However, on the base of the discussion in Section 3, it is easy to find out that the cross-bispectrum $b_{\ell_1 \ell_2 \ell_3}^{TEB}$ and all bispectra with an odd number of polarization terms are zero, i.e. $b_{\ell_1 \ell_2 \ell_3}^{EEE} = b_{\ell_1 \ell_2 \ell_3}^{TTE} = \dots = 0$. For the remaining two cases, the bispectrum is proportional to $b_{\ell_1 \ell_2 \ell_3}^{TTT}$ and it is given as:

$$b_{\ell_1 \ell_2 \ell_3}^{TEE} = b_{\ell_1 \ell_2 \ell_3}^{TBB} = \frac{1}{2} \langle p^2 \rangle b_{\ell_1 \ell_2 \ell_3}^{TTT}. \quad (20)$$

The total power spectrum and the bispectrum of the point sources are the two ingredients needed to provide an estimate of their impact on the primordial non-Gaussianity f_{nl} parameter. The shot-noise terms of TTT and TEE bispectra from radio and far-IR sources are shown in Fig. 4. The frequency at which far-IR sources equal or overcome the

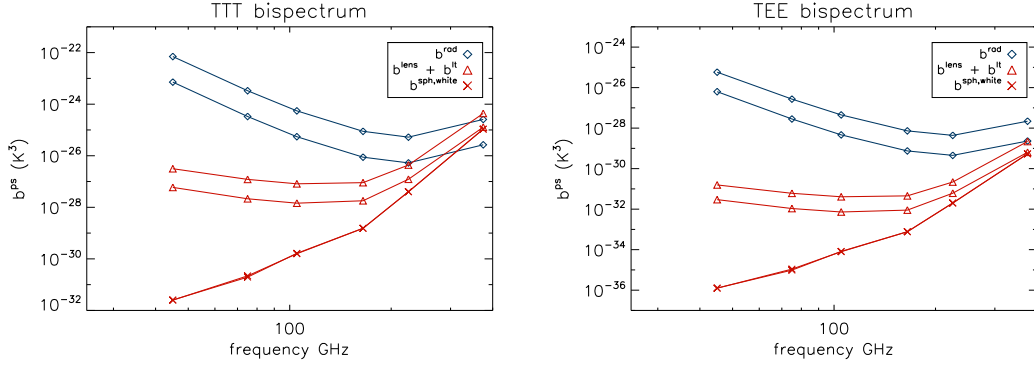


Figure 4. The amplitude of the shot-noise bispectrum of radio sources (b^{rad}) and of the far-IR source (for late-type plus lensed galaxies, b^{lt+le} , and for proto-spheroidal galaxies, $b^{sph,white}$) as a function of frequency and for the two considered flux density limits, i.e. $S_c = 0.3$ and 1 Jy. The left panel corresponds to the TTT bispectrum and the right panel corresponds to the TEE bispectrum.

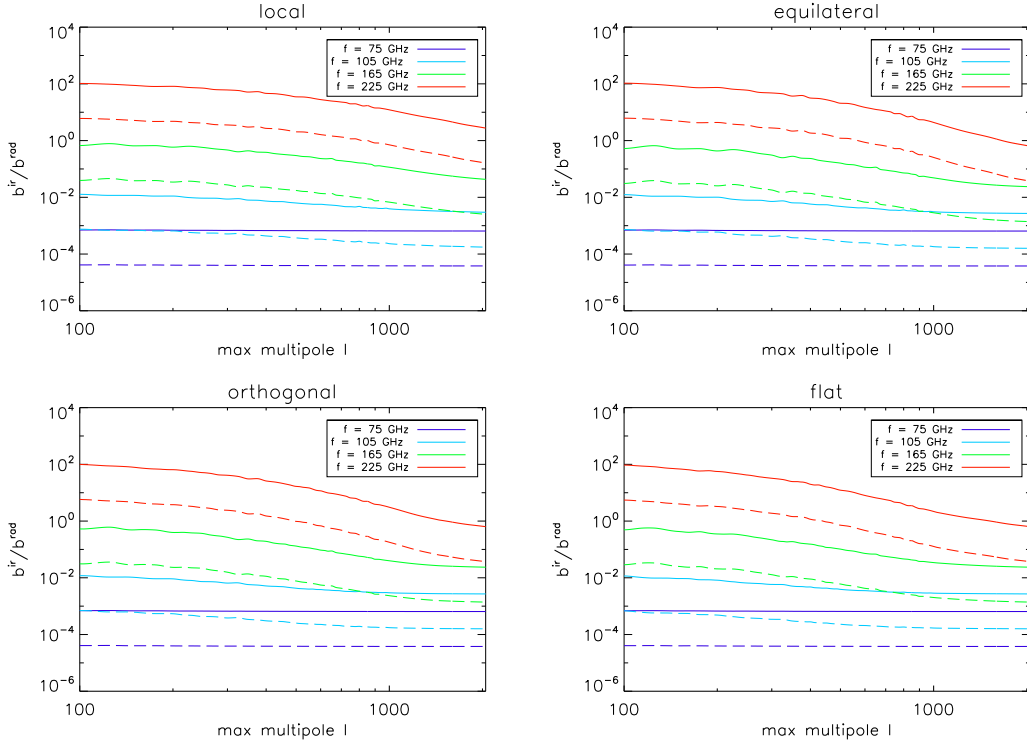


Figure 5. Ratio of the far-IR source bispectrum b^{ir} to the radio source bispectrum b^{rad} for $S_c = 0.3$ Jy and the 4 considered shapes: local configuration ($\ell_1 = \ell_2 = \ell$ and $\ell_3 = \ell_{min} = 2$), equilateral configuration ($\ell_1 = \ell_2 = \ell_3 = \ell$), isosceles orthogonal configuration ($\ell_1 = \ell_2 = \ell$ and $\ell_3 = \sqrt{2}\ell$) and isosceles flat configuration ($\ell_1 = \ell_2 = \ell$ and $\ell_3 = 2\ell$). The solid lines correspond to T, and the long dashed lines correspond to T and E.

ERS bispectrum is shifted to higher frequencies with respect to the power spectrum, i.e. it is around 300 (350) GHz for the *TTT* (*TEE*) bispectrum. This is in agreement with the fact that sources with flux density close to S_c give a larger contribution to the bispectrum than to the power spectrum. A significant dependence on the flux density limit is observed in the bispectrum of ERS and of late-type plus lensed galaxies, but not of proto-spheroidal galaxies.

Finally, we compare the total bispectrum of far-IR sources with the ERS one as a function of multipoles and for the four used configurations (see Fig. 5). The ratio is $\gtrsim 1$ only at 225 GHz for *TTT*, and for *TEE*, but at low multipoles. Otherwise, far-IR sources are always subdominant,

or even negligible, unless considering multipoles $\ell < 100$. As widely discussed in Sec. 3, clustering of far-IR sources becomes less relevant at low frequencies, and at $\nu \lesssim 100$ GHz the far-IR bispectrum is almost constant. Our Fig. 5 can be directly compared to Fig. 9 of Lacasa et al. (2012). Various differences can be highlighted from the two plots: 1) at high multipoles, the bispectrum ratio we find is typically higher than one order of magnitude; 2) far-IR bispectra by Lacasa et al. (2012) have a steeper slope; 3) no frequency dependence is observed in Lacasa et al. (2012) results. These discrepancies should be attributed to the different way to model far-IR sources and their correlation.

5.2 Bias and uncertainties on f_{nl}

Considering weak levels of non-Gaussianity, the bias induced in the primordial bispectrum $B_{\ell_1\ell_2\ell_3}^{prim}$ by the point-source bispectrum $B_{\ell_1\ell_2\ell_3}^{ps}$ is (see e.g. Komatsu & Spergel 2001; Bartolo et al. 2004; Yadav & Wandelt 2010; Lacasa et al. 2012; Martínez-González & Planck Collaboration 2012):

$$\Delta f_{nl} = \sigma^2(f_{nl}) \times \sum_{\ell_1 \leq \ell_2 \leq \ell_3 \leq \ell_{max}} \frac{B_{\ell_1\ell_2\ell_3}^{ps} B_{\ell_1\ell_2\ell_3}^{prim}}{(\Delta_{\ell_1\ell_2\ell_3} C_{\ell_1}^{tot} C_{\ell_2}^{tot} C_{\ell_3}^{tot})}, \quad (21)$$

where

$$C_{\ell}^{tot} = (C_{\ell}^{CMB} + C_{\ell}^{ps}) w_{\ell}^2 + C_{\ell}^{noise}, \quad (22)$$

C_{ℓ}^{CMB} is the CMB power spectrum, w_{ℓ} contains the instrumental and pixelization beams, C_{ℓ}^{noise} is the power spectrum of the noise, $\Delta_{\ell_1\ell_2\ell_3} = 1 + 2\delta_{\ell_1\ell_2}\delta_{\ell_2\ell_3} + \delta_{\ell_1\ell_2} + \delta_{\ell_2\ell_3} + \delta_{\ell_1\ell_3}$. The error-bar of the f_{nl} parameter is given by (Komatsu & Spergel 2001):

$$\sigma^{-2}(f_{nl}) = \sum_{\ell_1 \leq \ell_2 \leq \ell_3} \frac{(B_{\ell_1\ell_2\ell_3}^{prim})^2}{(\Delta_{\ell_1\ell_2\ell_3} C_{\ell_1}^{tot} C_{\ell_2}^{tot} C_{\ell_3}^{tot})}. \quad (23)$$

This estimator can be generalised to include the polarization:

$$\Delta f_{nl} = \sigma^2(f_{nl}) \times \sum_{ijklrst} \sum_{\ell_1 \leq \ell_2 \leq \ell_3 \leq \ell_{max}} (B_{\ell_1\ell_2\ell_3}^{ps})^{ijk} C_{ijk,rst}^{-1} (B_{\ell_1\ell_2\ell_3}^{prim})^{rst}, \quad (24)$$

where

$$\sigma^{-2}(f_{nl}) = \sum_{ijklrst} \sum_{\ell_1 \leq \ell_2 \leq \ell_3 \leq \ell_{max}} (B_{\ell_1\ell_2\ell_3}^{prim})^{ijk} C_{ijk,rst}^{-1} (B_{\ell_1\ell_2\ell_3}^{prim})^{rst}. \quad (25)$$

The covariance matrix $C_{ijk,rst}$ is given by (Yadav et al. 2007):

$$\begin{aligned} C_{ijk,prq} &= C_{\ell_1}^{ip} C_{\ell_2}^{jq} C_{\ell_3}^{kr} + C_{\ell_1}^{ip} C_{\ell_2}^{jr} C_{\ell_3}^{kq} \delta_{\ell_2\ell_3} + C_{\ell_1}^{iq} C_{\ell_2}^{jp} C_{\ell_3}^{kr} \delta_{\ell_1\ell_2} \\ &+ C_{\ell_1}^{ir} C_{\ell_2}^{jq} C_{\ell_3}^{kp} \delta_{\ell_1\ell_3} + C_{\ell_1}^{iq} C_{\ell_2}^{jr} C_{\ell_3}^{kp} \delta_{\ell_1\ell_2} \delta_{\ell_2\ell_3} \delta_{\ell_3\ell_1} \\ &+ C_{\ell_1}^{ir} C_{\ell_2}^{jp} C_{\ell_3}^{kq} \delta_{\ell_1\ell_3} \delta_{\ell_2\ell_1} \delta_{\ell_2\ell_3}. \end{aligned} \quad (26)$$

The indices $\{i, j, k, r, s, t\}$ cover the intensity T and the polarization E and B modes. The cosmological signal for the B mode is negligible. Including the point source B mode signal in the estimator does not improve the estimates of $\sigma(f_{nl})$ and $\Delta(f_{nl})$. Therefore we just include in the estimator the T and E modes for the case with polarization. As in the case with intensity only, each of the power or cross-power spectrum in Eq. (26) contain the CMB signal, instrumental beam, instrumental noise spectrum and the point source spectrum contributions.

6 RESULTS

We have studied the impact of unresolved point sources on the possible measurement of the f_{nl} parameter for two cases: a) an ideal experiment without instrumental beam nor instrumental noise; b) a possible future CORe-like mission, sensitive to temperature and polarization, with instrumental parameters adopted from The CORe Collaboration et al.

Table 1. Instrumental properties for a possible future CORe-like mission, based on values given by The CORe Collaboration et al. (2011).

ν (GHz)	45	75	105	165	225	375
FWHM (arcmin)	23.3	14.0	10.0	6.4	4.7	2.8
T RMS noise*	5.25	2.73	2.68	2.67	2.64	68.6
Pol. RMS noise*	9.07	4.72	4.63	4.61	4.57	119

* μK arcmin

(2011) and summarised in Table 1. The CMB power spectrum and transfer function for temperature and polarization needed to estimate the f_{nl} bias and its uncertainty (Eqs. 21, 23, 24 and 25) are numerically computed with CAMB (Lewis et al. 2000) using the cosmological parameters that best-fits WMAP 7-yr data. In this section we present results for the uncertainty on the f_{nl} parameter, $\sigma(f_{nl})$, for the expected bias, $\Delta(f_{nl})$, and for the relative bias, $\Delta(f_{nl})/\sigma(f_{nl})$ (see Fig. 6, Tables 2 and 3 for the ideal case, and Fig. 7, Tables 4 and 5 for a CORe-like mission). We compare results obtained with temperature only and with temperature plus polarization. Four different f_{nl} shapes are taken into account, i.e. local, equilateral, orthogonal and flat. Fig. 6 and 7 are for $S_c = 0.3$ Jy and for frequencies 75, 105, 165 and 225 GHz. In the Tables we also provide the results, evaluated at $\ell_{max} = 2048$, for $S_c = 1.0$ Jy and for 45 and 375 GHz.

The following results assume full sky. This is an unrealistic hypothesis as Galactic Plane and strong point sources have to be masked. How $\sigma(f_{nl})$ depends on the mask and on the fraction of the sky available, f_{sky} , is something complex and outside the purpose of this work. However, for large areas of the sky ($f_{sky} \gtrsim 0.7$) the following approximation can be used (Komatsu et al. 2002):

$$\sigma(f_{nl})_{cutsky} = \sigma(f_{nl})_{fullsky} / \sqrt{f_{sky}}. \quad (27)$$

The bias on f_{nl} does not depend on f_{sky} , as it can be seen from Eq. 21.

6.1 Uncertainty

In Eqs. 23 and 25 of the previous section we have provided the analytical formulas to estimate the uncertainty on the f_{nl} parameter. As we can see, the point sources contribution enters only in the total angular power spectrum (Eq. 22), in the sum $C_{\ell}^{CMB} + C_{\ell}^{ps}$. In the frequency range 75–225 GHz, C_{ℓ}^{ps} is always subdominant with respect to T and E-mode CMB spectra up to $\ell \sim 2000$ (see Fig. 2). Therefore, as illustrated by Fig. 6 and 7, the impact of point sources on the uncertainty in the determination of the f_{nl} parameter is small or negligible, especially when polarization is considered. In this case, in fact, $\sigma(f_{nl})$ is almost indistinguishable with the intrinsic f_{nl} uncertainty due to the cosmic variance (black curves in the plots, indicated as “no sources”). This is true also for the “temperature only” case at 105 and 165 GHz, i.e. the frequencies where the signal from point sources is minimum. At 75 GHz the uncertainty becomes slightly higher only at $\ell \gtrsim 1500$ because of the increasing contribution of ERS; while, a larger $\sigma(f_{nl})$ is obtained at 225 GHz in the all range of ℓ s, clearly due to the clustered signal of IR sources. At 353 GHz the point sources contamination grows dramatically, and the $\sigma(f_{nl})$ is around 4–6

Table 2. The expected uncertainty $\sigma(f_{nl})$, bias Δf_{nl} and relative bias $\Delta f_{nl}/\sigma(f_{nl})$ at $\ell_{max} = 2048$ from temperature only and temperature plus polarization for an ideal mission. $S_c = 0.3$ Jy is adopted.

	case	T	T	T	T	T	T	T+E	T+E	T+E	T+E	T+E	T+E
	Freq.	45	75	105	165	225	375	45	75	105	165	225	375
local	$\sigma(f_{nl})$	7.4	4.9	4.4	4.2	5.2	29.7	2.8	2.3	2.1	2.1	2.3	3.3
	Δf_{nl}	82.1	10.3	2.1	0.4	0.7	25.6	-9.7	-2.6	-0.6	-0.1	-0.1	-0.1
	$\Delta f_{nl}/\sigma(f_{nl})$	11.1	2.1	0.5	0.1	0.1	0.9	-3.5	-1.1	-0.3	-0.1	-0.1	-0.0
equilateral	$\sigma(f_{nl})$	75.4	60.4	56.8	55.9	65.1	232.4	24.0	20.3	19.5	19.2	21.1	35.3
	Δf_{nl}	4629.3	599.9	107.2	17.2	49.1	950.7	480.2	54.5	7.3	0.8	4.0	17.9
	$\Delta f_{nl}/\sigma(f_{nl})$	61.4	9.9	1.9	0.3	0.8	4.1	20.0	2.7	0.4	0.0	0.2	0.5
orthogonal	$\sigma(f_{nl})$	40.1	29.7	27.4	26.8	32.0	139.0	11.6	9.8	9.4	9.2	10.1	16.5
	Δf_{nl}	955.5	51.7	2.5	-0.2	9.7	371.4	308.7	48.3	9.4	1.6	3.4	7.2
	$\Delta f_{nl}/\sigma(f_{nl})$	23.8	1.7	0.1	-0.0	0.3	2.7	26.7	4.9	1.0	0.2	0.3	0.4
flat	$\sigma(f_{nl})$	73.7	53.3	49.0	47.9	57.6	284.7	20.6	17.4	16.6	16.4	17.9	29.1
	Δf_{nl}	598.6	150.5	36.0	6.7	3.4	-66.0	-311.6	-56.3	-12.2	-2.2	-3.9	-5.2
	$\Delta f_{nl}/\sigma(f_{nl})$	8.1	2.8	0.7	0.1	0.1	-0.2	-15.1	-3.2	-0.7	-0.1	-0.2	-0.2

Table 3. The expected uncertainty $\sigma(f_{nl})$, bias Δf_{nl} and relative bias $\Delta f_{nl}/\sigma(f_{nl})$ at $\ell_{max} = 2048$ from temperature only and temperature plus polarization for an ideal mission. $S_c = 1$ Jy is adopted.

	case	T	T	T	T	T	T	T+E	T+E	T+E	T+E	T+E	T+E
	Freq.	45	75	105	165	225	375	45	75	105	165	225	375
local	$\sigma(f_{nl})$	9.9	5.9	4.9	4.4	5.3	29.8	3.2	2.5	2.3	2.1	2.3	3.3
	Δf_{nl}	351.1	68.5	17.6	3.4	2.3	25.6	-5.9	-12.6	-4.4	-1.0	-0.5	-0.1
	$\Delta f_{nl}/\sigma(f_{nl})$	35.6	11.6	3.6	0.8	0.4	0.9	-1.9	-5.1	-2.0	-0.5	-0.2	-0.0
equilateral	$\sigma(f_{nl})$	88.7	66.6	59.9	57.0	65.6	229.8	27.7	21.8	20.2	19.5	21.2	35.3
	Δf_{nl}	17689.6	4075.1	1017.5	174.2	135.5	948.9	2226.3	390.7	90.7	11.5	10.8	20.5
	$\Delta f_{nl}/\sigma(f_{nl})$	199.4	61.2	17.0	3.1	2.1	4.1	80.4	17.9	4.5	0.6	0.5	0.6
orthogonal	$\sigma(f_{nl})$	50.2	33.8	29.3	27.5	32.3	138.6	13.4	10.5	9.7	9.4	10.1	16.5
	Δf_{nl}	5411.3	573.7	80.9	3.6	16.4	377.8	1007.2	297.6	82.1	15.1	9.3	7.1
	$\Delta f_{nl}/\sigma(f_{nl})$	107.8	17.0	2.8	0.1	0.5	2.7	75.3	28.4	8.5	1.6	0.9	0.4
flat	$\sigma(f_{nl})$	94.6	61.3	52.7	49.2	58.2	284.5	23.8	18.6	17.3	16.6	18.0	29.2
	Δf_{nl}	455.7	784.2	263.4	59.1	26.6	-69.0	-770.4	-326.8	-96.4	-19.6	-10.8	-4.1
	$\Delta f_{nl}/\sigma(f_{nl})$	4.8	12.8	5.0	1.2	0.5	-0.2	-32.4	-17.5	-5.6	-1.2	-0.6	-0.1

times higher than at 225 GHz. On the other hand, the loss of sensitivity between 75 and 45 GHz is not so strong, due to the flatter spectral behaviour of ERS. These results seem to be quite independent of the two flux density limits considered, even at 45 and 75 GHz, where $\sigma(f_{nl})$ is about 10–20% larger (see Table 2–5).

When polarization is taken into account, f_{nl} error-bars are reduced approximately by a factor of 2–3 accordingly to the shape, in the frequency range 75–225 GHz. At 45 and 375 GHz, polarization permits to achieve a very large improvement in the f_{nl} error-bars, but only for the ideal case. In a CORe-like mission the instrumental noise in polarization saturates the f_{nl} error-bars at these frequencies and prevents to reduce them as in the ideal case.

The values of $\sigma(f_{nl})$ obtained from a CORe-like mission are very close to the results of the ideal case. This means that observational performances, in terms of instrumental noise and beam, given in Table 1, are almost optimal for f_{nl} measurements, at least up to $\ell \sim 2000$. Only in the 75–GHz channel (and partially in the 105–GHz channel) the effect of the beam is observed in Fig. 7, where $\sigma(f_{nl})$ starts to be constant at $\ell_{max} \gtrsim 1500$. In the 165– and 225–GHz channels the

f_{nl} uncertainty is always decreasing up to $\ell_{max} = 2048$. Note however that this is not the case in a Planck-like mission, where the noise contamination in the E mode is more important and the improvement from T only to T and polarization is 20–30% (Martínez-González & Planck Collaboration 2012).

6.2 Bias

As expected, the bias (or the relative bias, shown in Fig. 6 and 7) rapidly increases with ℓ_{max} . Its value is also strongly dependent on the frequency. In fact, for example in the case of no clustering, the bias is directly proportional to the amplitude of the shot-noise bispectrum of point sources (see Eq. 21).

If we consider only temperature and $S_c = 0.3$ Jy, the bias is practically negligible at 165 and 225 GHz (i.e. where $\ell_{\ell_1 \ell_2 \ell_3}^{ps, white}$ is minimum) for the local, orthogonal and flat shapes. The relative bias is less than 1 also for the equilateral shape, which is the shape most affected by point sources. As for $\sigma(f_{nl})$, the bias strongly increases at 375 GHz, be-

ing typically more than one order of magnitude higher than at 225 GHz. At 105 GHz it is still small, with a relative value less than 1 (apart from the equilateral shape, with $\Delta f_{nl} = 107$). At lower frequencies, however, $\Delta f_{nl} \gg \sigma(f_{nl})$.

Moreover, we find that Δf_{nl} for the local, equilateral and flat shapes is negative, although negligible, at low multipoles ($\ell \leq 200$) and it becomes positive at higher multipoles⁹. The bias for the orthogonal shape is oscillating around zero and therefore, in this case, there are certain multipoles where $\Delta f_{nl} \simeq 0$.

It is interesting to notice that when instrumental noise and beam function are introduced, the bias (and the relative bias) are equal or even lower than in the ideal case at $\ell_{max} = 2048$. One simple explanation is that the beam and the noise prevent the high- ℓ terms in the sum of Eq. 21 and 24 to diverge.

When the polarization is considered, the bias suffers important variations for each different shape in its amplitude and its sign. This is dependent on the extra terms in the estimator: the E-mode primordial bispectrum, the E-mode point source bispectrum and also the inverse of the covariance matrix in Eq. 26. The bias of the local and flat shapes becomes negative, whereas in the equilateral and orthogonal shapes it keeps a positive value. The local and flat shapes bias are also reduced in amplitude but the strongest improvement is for the equilateral shape. On the contrary, at certain frequencies the amplitude of the bias of the orthogonal shape increases compared with the case of temperature only (see Tables 2 and 3). Finally, it can be noticed that the amplitude of the bias is typically lower in a CORe-like mission than in the ideal case, as effect of considering instrumental properties in Eq. 21 and 24.

7 CONCLUSIONS

In this paper we present a full set of forecasts on the contamination produced by unresolved extragalactic point sources on the primordial non-Gaussianity f_{nl} parameter – hopefully detectable by the analysis of future high-resolution CMB (all-sky and low-noise) anisotropy maps – in the frequency interval 45–375 GHz. We have considered two scenarios: a) an ideal case without instrumental noise nor instrumental beams; b) a future experiment with CORe-like instrumental parameters. We have characterized all source populations relevant in this frequency interval by using two recently published models: the Tucci et al. (2011) model for extragalactic radio sources and the Lapi et al. (2011) model for far-IR/sub-mm sources. It is important to remind here that these two models have proved very successful in the explanation of all of the most recent and published results on number counts (and on other relevant statistics) of extragalactic point sources in the frequency range from ~ 30 to ~ 1000 GHz.

As a first step, the angular power spectrum and bispectrum due to unresolved extragalactic point sources for both temperature and polarization have been estimated and

compared. According to the above quoted models, the contaminating signal produced by far-IR/sub-mm selected extragalactic sources starts to dominate over the ERS one at $\nu \gtrsim 200$ GHz in the temperature (or total intensity) angular power spectrum and bispectrum. In spite of their very low (average) level of polarized emission, this source population is also relevant in polarization, especially at large scales, due to the enhanced signal produced by the strong clustering of high- z far-IR/sub-m spheroidal galaxies. On the contrary, their effect is completely negligible at frequencies $\lesssim 100$ GHz. On the other hand, unresolved ERS constitute a more relevant contaminant in all the frequency range considered here and, thus, their effect on the CMB anisotropy signal has to be properly modeled, for a correct evaluation of their impact. In any case, their signal is found to be dominant over the intrinsic CMB one only at frequencies below 75 GHz, thus out of the CMB cosmological window.

We have studied the expected impact of undetected point sources on the f_{nl} parameter in terms of uncertainty and bias, for the local, equilateral, orthogonal and flat shapes. For a CORe-like mission, we find out that the best frequency for a f_{nl} analysis is ~ 165 GHz. At this frequency (and $S_c = 0.3$ Jy), the effect of unresolved point sources on the accuracy in the determination of f_{nl} is almost negligible. The uncertainty on f_{nl} does not significantly change whether or not their contribution is included, and estimated values of f_{nl} are essentially unbiased (apart from the equilateral shape for which $\Delta f_{nl}/\sigma(f_{nl}) \sim 0.3$ at $\ell_{max} = 2048$). At the frequencies 75 and 105 GHz, results are similar to 165-GHz ones for the $\sigma(f_{nl})$, but f_{nl} can be significantly biased, mainly for the equilateral and the flat shape; on the other hand, at 225 GHz we observe an increase in the f_{nl} error-bars. If we move far from this frequency range the capability of an accurate f_{nl} measurement fast degrades, especially if only temperature is used.

When polarization is considered, error-bars in the f_{nl} estimate are reduced by at least a factor 2 for the ideal case (in agreement with estimates in literature; see e.g. Babich et al. 2004) and they are not affected by point sources in all the frequency range 75–225 GHz. Moreover, polarization can also help to significantly reduce the bias induced by unresolved sources. As example, for the equilateral shape, i.e. the shape most affected by point sources, the bias is a factor from 3 to 10 lower than from temperature only analysis. We can say therefore that polarization allows to expand the best range of frequencies where f_{nl} can be safely determined.

Discrepancies in the far-IR source bispectrum are observed when compared with Lacasa et al. (2012). They are attributed to the different ways to model the far-IR sources (see Section 5). This dependency might affect the bias for the considered shapes especially at high frequencies (see Section 6).

Finally, as expected, the bias induced by point sources is strongly related to the flux density limit down to which sources are detected and removed/masked. Our results seem to point out that $S_c = 0.3$ Jy is low enough to have unbiased f_{nl} values at least at 165 and 225 GHz for a CORe-like mission. At different frequencies, lower flux density limits are required. On the other hand, f_{nl} uncertainty is weakly affected by the choice of S_c because it is dominated by the intrinsic f_{nl} variance (i.e. independent of contaminants), that

⁹ This change in the sign of the “local” bias is not found in Lacasa et al. (2012), where the bias due to IR sources is still negative at $\ell = 700$ and 2048. This different result may be dependent on the actual details of the characterization of the IR sources.

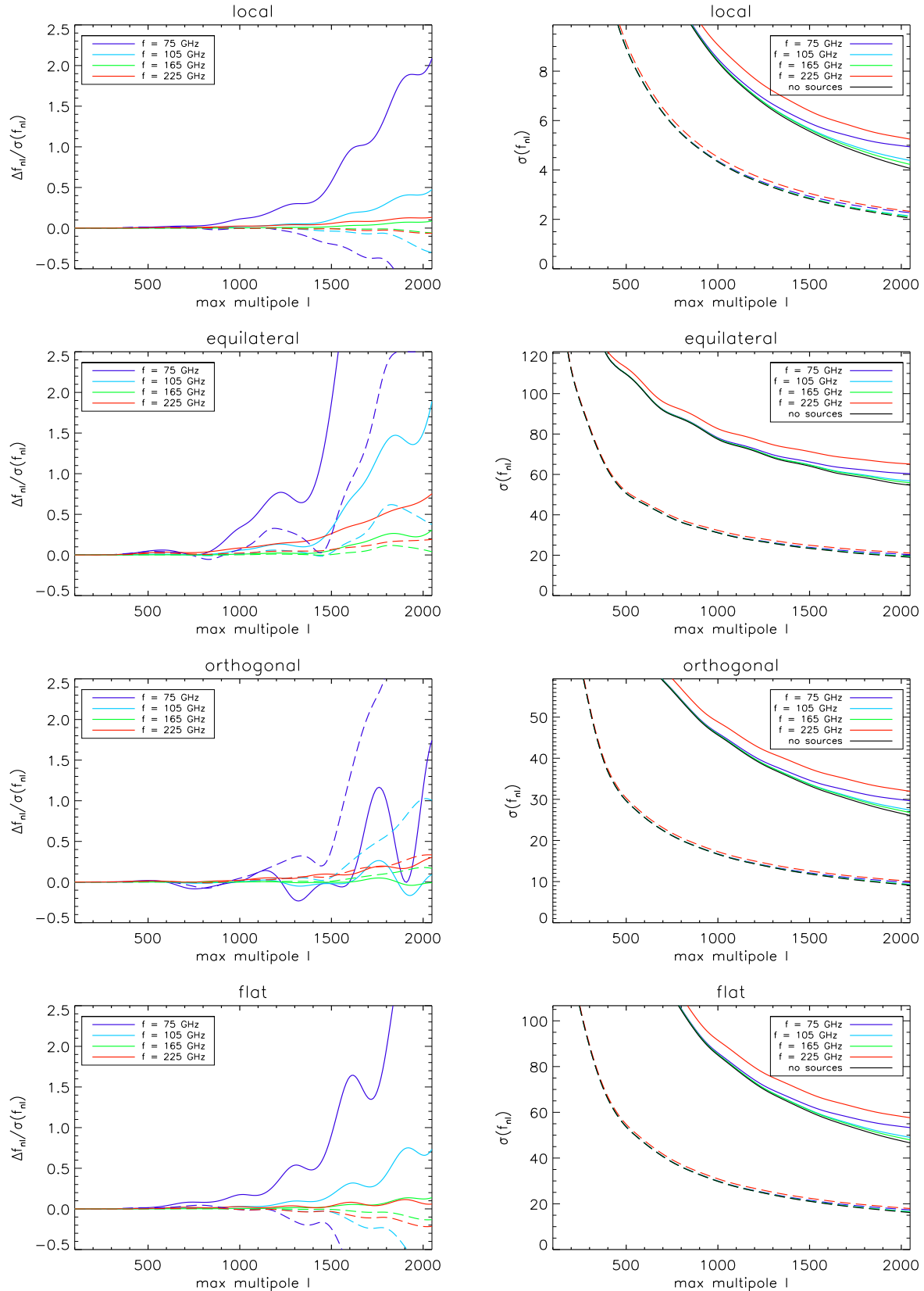


Figure 6. From left to right: the relative bias $\Delta(f_{nl})/\sigma(f_{nl})$ and the f_{nl} uncertainty $\sigma(f_{nl})$ produced by unresolved point sources as a function of l_{max} for the ideal case. We consider the flux density limit $S_c = 0.3$ Jy and the following frequencies: 75, 105, 165, 225 GHz and the configuration without point sources (black line in right panels). From top to bottom, we plot results for the local, equilateral, orthogonal and flat f_{nl} shapes. The solid lines take into account only temperature, while the long dashed lines include temperature and polarization.

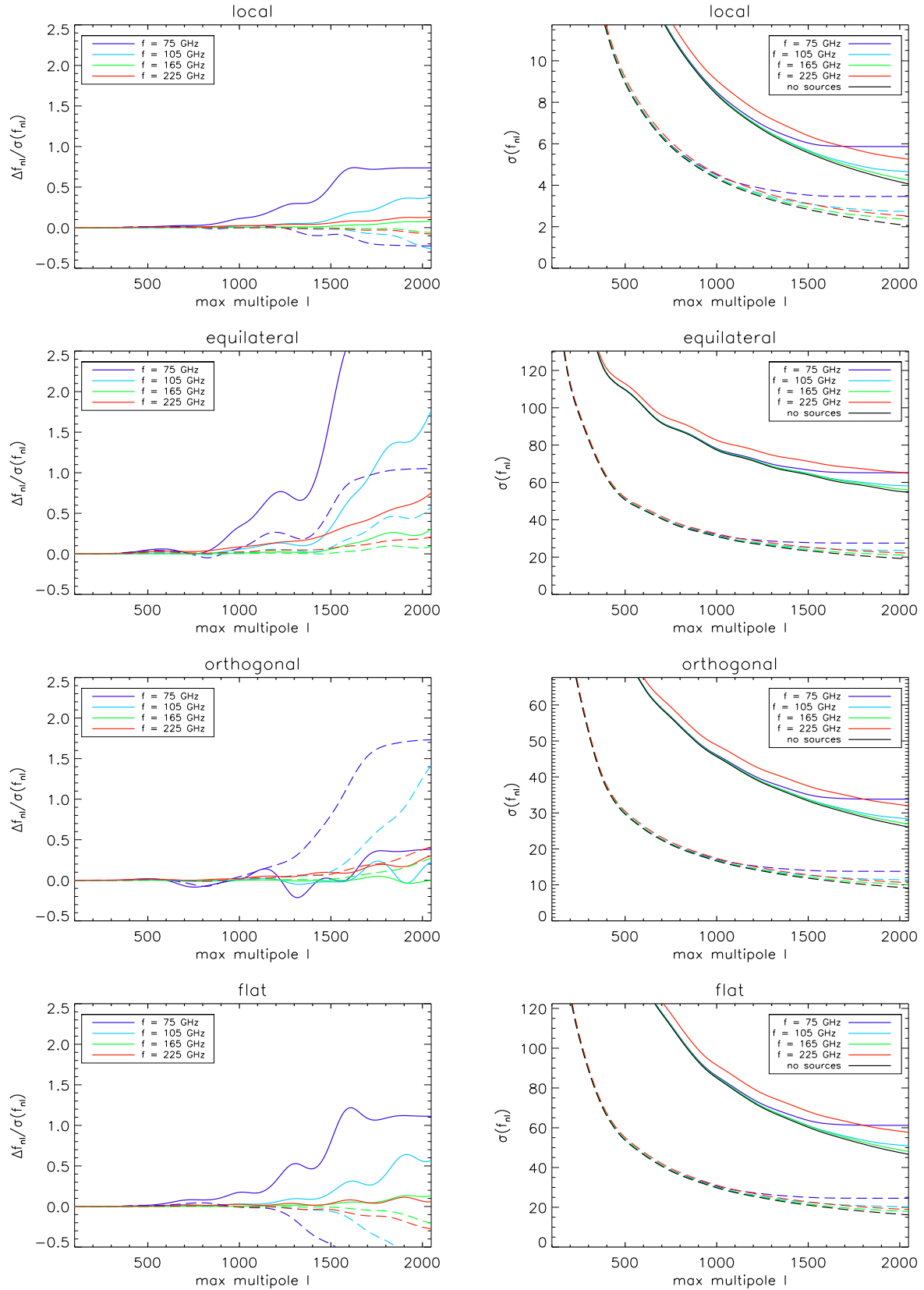


Figure 7. As in Fig. 6 but for a CORE-like mission.

Table 4. The expected uncertainty $\sigma(f_{nl})$, bias Δf_{nl} and relative bias $\Delta f_{nl}/\sigma(f_{nl})$ at $\ell_{max} = 2048$ from temperature only and temperature plus polarization for a CORe-like mission. $S_c = 0.3$ Jy is adopted.

	case	T	T	T	T	T	T	T+E	T+E	T+E	T+E	T+E	T+E
	Freq.	45	75	105	165	225	375	45	75	105	165	225	375
local	$\sigma(f_{nl})$	9.7	5.9	4.7	4.2	5.3	29.8	6.0	3.5	2.7	2.3	2.5	20.6
	Δf_{nl}	16.0	4.3	1.8	0.4	0.7	25.1	1.9	-0.8	-0.7	-0.1	-0.2	8.2
	$\Delta f_{nl}/\sigma(f_{nl})$	1.7	0.7	0.4	0.1	0.1	0.8	0.3	-0.2	-0.3	-0.1	-0.1	0.4
equilateral	$\sigma(f_{nl})$	84.3	65.2	58.1	56.0	65.2	232.6	41.1	27.5	23.5	21.0	22.2	147.2
	Δf_{nl}	421.9	202.4	102.7	17.5	49.0	935.9	66.2	28.9	13.5	1.9	4.6	343.8
	$\Delta f_{nl}/\sigma(f_{nl})$	5.0	3.1	1.8	0.3	0.8	4.0	1.6	1.1	0.6	0.1	0.2	2.3
orthogonal	$\sigma(f_{nl})$	49.7	33.8	28.4	26.9	32.0	139.1	21.7	13.8	11.4	10.1	10.6	82.0
	Δf_{nl}	39.9	12.9	6.5	-0.1	9.7	367.8	12.1	23.8	16.1	2.8	4.4	130.2
	$\Delta f_{nl}/\sigma(f_{nl})$	0.8	0.4	0.2	-0.0	0.3	2.6	0.6	1.7	1.4	0.3	0.4	1.6
flat	$\sigma(f_{nl})$	93.8	61.2	50.9	48.1	57.7	285.1	39.1	24.5	20.2	17.9	18.9	148.1
	Δf_{nl}	190.3	68.1	29.0	6.5	3.4	-68.8	10.4	-26.3	-20.4	-3.7	-5.2	-38.4
	$\Delta f_{nl}/\sigma(f_{nl})$	2.0	1.1	0.6	0.1	0.1	-0.2	0.3	-1.1	-1.0	-0.2	-0.3	-0.3

Table 5. The expected uncertainty $\sigma(f_{nl})$, bias Δf_{nl} and relative bias $\Delta f_{nl}/\sigma(f_{nl})$ at $\ell_{max} = 2048$ from temperature only and temperature plus polarization for CORe-like mission. $S_c = 1$ Jy is adopted.

	case	T	T	T	T	T	T	T+E	T+E	T+E	T+E	T+E	T+E
	Freq.	45	75	105	165	225	375	45	75	105	165	225	375
local	$\sigma(f_{nl})$	11.1	6.4	5.0	4.4	5.3	29.9	6.6	3.7	2.9	2.4	2.5	20.6
	Δf_{nl}	130.7	37.1	15.6	3.4	2.3	25.0	15.3	-7.0	-6.0	-1.2	-0.6	8.1
	$\Delta f_{nl}/\sigma(f_{nl})$	11.8	5.8	3.1	0.8	0.4	0.8	2.3	-1.9	-2.1	-0.5	-0.2	0.4
equilateral	$\sigma(f_{nl})$	92.4	68.9	60.6	57.1	65.7	230.0	43.7	28.4	24.0	21.2	22.3	146.3
	Δf_{nl}	3428.4	1731.9	916.2	175.0	135.3	933.6	515.4	235.0	117.5	19.5	12.6	346.7
	$\Delta f_{nl}/\sigma(f_{nl})$	37.1	25.1	15.1	3.1	2.1	4.1	11.8	8.3	4.9	0.9	0.6	2.4
orthogonal	$\sigma(f_{nl})$	55.3	36.2	30.0	27.5	32.3	138.7	23.3	14.3	11.7	10.2	10.7	81.8
	Δf_{nl}	553.1	161.5	79.9	4.4	16.4	374.0	110.3	202.6	136.9	25.4	12.2	132.5
	$\Delta f_{nl}/\sigma(f_{nl})$	10.0	4.5	2.7	0.2	0.5	2.7	4.7	14.2	11.7	2.5	1.1	1.6
flat	$\sigma(f_{nl})$	105.8	65.8	53.9	49.3	58.3	284.9	42.0	25.5	20.8	18.1	19.0	147.7
	Δf_{nl}	1232.1	523.1	232.3	58.3	26.5	-72.1	59.4	-227.2	-172.4	-33.0	-14.7	-39.3
	$\Delta f_{nl}/\sigma(f_{nl})$	11.6	7.9	4.3	1.2	0.5	-0.3	1.4	-8.9	-8.3	-1.8	-0.8	-0.3

decreases when increasing ℓ_{max} . We want to stress the importance of high-resolution (i.e., FWHM < 10 arcmin) and polarization-sensitive instruments, in order to have significant improvements in the precision of primordial f_{nl} in future experiments beyond Planck.

ACKNOWLEDGMENTS

The authors acknowledge partial financial support from the Spanish Ministerio de Economía y Competitividad projects AYA2010-21766-C03-01, AYA-2012-39475-C02-01 and the Consolider Ingenio-2010 Programme project CSD2010-00064. JGN acknowledges financial support from the Spanish National Research Council (CSIC) for a JAE-DOC fellowship. MLC thanks the Spanish Ministerio de Economía y Competitividad for a Juan de la Cierva fellowship. AC acknowledges the CSIC and the Spanish Ministerio de Educación, Cultura y Deporte for a postdoctoral fellowship at the Cavendish Laboratory of the University of Cambridge (UK). The authors acknowledge the computer resources, technical expertise and assistance provided by the Spanish

Supercomputing Network (RES) nodes at Universidad de Cantabria and Universidad Politécnica de Madrid. We also acknowledge the use of LAMBDA, support for which is provided by the NASA Office of Space Science. We have also used the software package HEALPix (Górski et al. 2005).

REFERENCES

- Agudo I., Thum C., Wiesemeyer H., Krichbaum T. P., 2010, ApJS, 189, 1
 Albrecht A., Steinhardt P. J., 1982, Physical Review Letters, 48, 1220
 Amblard A., Cooray A., Serra P., Temi P., Barton E., et al. 2010, A&A, 518, L9
 Amblard A., Cooray A., Serra P., Altieri B., Arumugam V., et al. 2011, Nature, 470, 510
 Angel J. R. P., Stockman H. S., 1980, A&AA, 18, 321
 Argüeso F., González-Nuevo J., Toffolatti L., 2003, ApJ, 598, 86
 Argüeso F., Sanz J. L., Barreiro R. B., Herranz D., González-Nuevo J., 2006, MNRAS, 373, 311

- Arkani-Hamed N., Creminelli P., Mukohyama S., Zaldarriaga M., 2004, *JCAP*, 4, 1
- Babich D., 2005, *Phys. Rev. D.*, 72, 043003
- Babich D., Creminelli P., Zaldarriaga M., 2004, *JCAP*, 8, 9
- Babich D., Pierpaoli E., 2008, *Phys. Rev. D.*, 77, 123011
- Bartolo N., Komatsu E., Matarrese S., Riotto A., 2004, *Phys. Rep.*, 402, 103
- Bartolo N., Matarrese S., Riotto A., 2010, *Advances in Astronomy*, Volume 2010, Article ID 157079.
- Bartolo N., Fasiello M., Matarrese S., Riotto A., 2010b, *JCAP*, 8, 8
- Battye R. A., Browne I. W. A., Peel M. W., Jackson N. J., Dickinson C., 2011, *MNRAS*, 413, 132
- Blain A. W., 1996, *MNRAS*, 283, 1340
- Blandford R. D., Königl A., 1979, *ApJ*, 232, 34
- Chen X., Huang M.-x., Kachru S., Shiu G., 2007, *Journal of Cosmology and Astroparticle Physics*, 1, 2
- Cheung C., Fitzpatrick A. L., Kaplan J., Senatore L., Creminelli P., 2008, *Journal of High Energy Physics*, 3, 14
- Creminelli P., Nicolis A., Senatore L., Tegmark M., Zaldarriaga M., 2006, *JCAP*, 5, 4
- Curto A., Martínez-González E., Barreiro R. B., 2012, *MNRAS*, 426, 1361
- Curto A., Martínez-González E., Barreiro R. B., Hobson M. P., 2011, *MNRAS*, 417, 488
- de Zotti G., Ricci R., Mesa D., Silva L., Mazzotta P., Toffolatti L., González-Nuevo J., 2005, *A&A*, 431, 893
- Delabrouille J., Betoule M., Melin J.-B., Miville-Deschênes M.-A., Gonzalez-Nuevo J., et al 2012, (arXiv:1207.3675)
- Dotson J. L., Vaillancourt J. E., Kirby L., Dowell C. D., Hildebrand R. H., Davidson J. A., 2010, *ApJS*, 186, 406
- Dunkley J., Hlozek R., Sievers J., Acquaviva V., Ade P. A. R., et al. 2011, *ApJ*, 739, 52
- Dunne L., Gomez H. L., da Cunha E., Charlot S., Dye S., et al 2011, *MNRAS*, 417, 1510
- Dvali G., Gruzinov A., Zaldarriaga M., 2004, *Phys. Rev. D.*, 69, 023505
- Eales S., Dunne L., Clements D., Cooray A., de Zotti G., et al. 2010, *Publications of the Astronomical Society of the Pacific*, 122, 499
- Fergusson J. R., Liguori M., Shellard E. P. S., 2010a, *Phys. Rev. D*, 82, 023502
- Fergusson J. R., Liguori M., Shellard E. P. S., 2010b, preprint (arXiv:1006.1642)
- González-Nuevo J., Lapi A., Fleuren S., Bressan S., Danese L., et al. 2012, *ApJ*, 749, 65
- González-Nuevo J., Massardi M., Argüeso F., Herranz D., Toffolatti L., Sanz J. L., López-Cañiego M., de Zotti G., 2008, *MNRAS*, 384, 711
- González-Nuevo J., Toffolatti L., Argüeso F., 2005, *ApJ*, 621, 1
- Górski K. M., Hivon E., Banday A. J., Wandelt B. D., Hansen F. K., Reinecke M., Bartelmann M., 2005, *ApJ*, 622, 759
- Granato G. L., De Zotti G., Silva L., Bressan A., Danese L., 2004, *ApJ*, 600, 580
- Granato G. L., Silva L., Monaco P., Panuzzo P., Salucci P., De Zotti G., Danese L., 2001, *MNRAS*, 324, 757
- Guo Q., Cole S., Lacey C. G., Baugh C. M., Frenk C. S., et al 2011, *MNRAS*, 412, 2277
- Guth A. H., 1981, *Phys. Rev. D*, 23, 347
- Hall N. R., Keisler R., Knox L., Reichardt C. L., Ade P. A. R., et al. 2010, *ApJ*, 718, 632
- Komatsu E., Smith K. M., Dunkley J., Bennett C. L., Gold B., et al. 2011, *ApJS*, 192, 18
- Komatsu E., 2010, *Classical and Quantum Gravity*, 27, 124010
- Komatsu E., Dunkley J., Nolta M. R., Bennett C. L., Gold B., Hinshaw G., Jarosik N., Larson D., Limon M., Page L., Spergel D. N., Halpern M., Hill R. S., Kogut A., Meyer S. S., Tucker G. S., Weiland J. L., Wollack E., Wright E. L., 2009, *ApJS*, 180, 330
- Komatsu E., Spergel D. N., Wandelt B. D., 2005, *ApJ*, 634, 14
- Komatsu E., Wandelt B. D., Spergel D. N., Banday A. J., Górski K. M., 2002, *ApJ*, 566, 19
- Komatsu E., Spergel D. N., 2001, *Phys. Rev. D*, 63, 063002
- Lacasa F., Aghanim N., Kunz M., Frommert M., 2012, *MNRAS*, 421, 1982
- Langlois D., Renaux-Petel S., Steer D. A., Tanaka T., 2008, *Phys. Rev. D.*, 78, 063523
- Lapi A., González-Nuevo J., Fan L., Bressan A., De Zotti G., Danese L., et al. 2011, *ApJ*, 742, 24
- Lapi A., Shankar F., Mao J., Granato G. L., Silva L., De Zotti G., Danese L., 2006, *ApJ*, 650, 42
- Lapi A., Kawakatu N., Bosnjak Z., Celotti A., Bressan A., Granato G. L., Danese L., 2008, *MNRAS*, 386, 608
- Lapi A., Negrello M., González-Nuevo J., Cai Z.-Y., De Zotti G., Danese L., 2012, *ApJ*, 755, 46
- Lewis A., Challinor A., Lasenby A., 2000, *ApJ*, 538, 473
- Liguori M., Sefusatti E., Fergusson J. R., Shellard E. P. S., 2010, *Advances in Astronomy*, Volume 2010, Article ID 980523.
- Lima M., Jain B., Devlin M., 2010, *MNRAS*, 406, 2352
- Lin C., 2009, preprint (arXiv:0908.4168)
- Linde A. D., 1982, *Physics Letters B*, 108, 389
- Linde A. D., 1983, *Physics Letters B*, 129, 177
- López-Cañiego M., González-Nuevo J., Massardi M., Bonavera L., Herranz D., et al 2012, (arXiv:1205.1929)
- Lyth D. H., Ungarelli C., Wands D., 2003, *Phys. Rev. D*, 67, 023503
- Maddox S. J., Dunne L., Rigby E., Eales S., Cooray A., et al. 2010, *A&A*, 518, L11
- Massardi M., Bonaldi A., Negrello M., Ricciardi S., Raccanelli A., de Zotti G., 2010, *MNRAS*, 404, 532
- Mao J., Lapi A., Granato G. L., de Zotti G., Danese L., 2007, *ApJ*, 667, 655
- Marriage T. A., Baptiste Juin J., Lin Y.-T., Marsden D., Nolta M. R., et al. 2011, *ApJ*, 731, 100
- Martínez-González E., Planck Collaboration 2012, in Beltrán Jiménez J., Ruiz Cembranos J. A., Dobado A., López Maroto A., De la Cruz Dombriz A., eds, *American Institute of Physics Conference Series Vol. 1458 of American Institute of Physics Conference Series*, The Planck mission and the cosmological paradigm. pp 190–206
- Meerburg P. D., van der Schaar J. P., Stefano Corasaniti P., 2009, *JCAP*, 5, 18
- Mukhanov V. F., Feldman H. A., Brandenberger R. H., 1992, *Phys. Rep.*, 215, 203
- Murphy T., Sadler E. M., Ekers R. D., Massardi M., Hancock P. J., et al. 2010, *MNRAS*, 402, 2403
- Negrello M., Hopwood R., De Zotti G., Cooray A., Verma

- A., et al. 2010, *Science*, 330, 800
- Negrello M., Perrotta F., González-Nuevo J., Silva L., de Zotti G., Granato G. L., Baccigalupi C., Danese L., 2007, *MNRAS*, 377, 1557
- Paciga G., Scott D., Chapin E. L., 2009, *MNRAS*, 395, 1153
- Perrotta F., Baccigalupi C., Bartelmann M., De Zotti G., Granato G. L., 2002, *MNRAS*, 329, 445
- Perrotta F., Magliocchetti M., Baccigalupi C., Bartelmann M., De Zotti G., Granato G. L., Silva L., Danese L., 2003, *MNRAS*, 338, 623
- Pilbratt G. L., Riedinger J. R., Passvogel T., Crone G., Doyle D., Gageur U., Heras A. M., Jewell C., Metcalfe L., Ott S., Schmidt M., 2010, *A&A*, 518, L1
- Planck Collaboration VII 2011, *A&A*, 536, A7
- Planck Collaboration VII 2013, *A&A*, 550, A133
- Planck Collaboration XIII 2011, *A&A*, 536, A13
- Planck Collaboration XV 2011, *A&A*, 536, A15
- Planck Collaboration XVIII 2011, *A&A*, 536, A18
- Refregier A., Spergel D. N., Herbig T., 2000, *ApJ*, 531, 31
- Sadler E. M., Ricci R., Ekers R. D., Sault R. J., Jackson C. A., de Zotti G., 2008, *MNRAS*, 385, 1656
- Sajina A., Partridge B., Evans T., Steff S., Vechik N., Myers S., Dicker S., Korngut P., 2011, *ApJ*, 732, 45
- Senatore L., Smith K. M., Zaldarriaga M., 2010, *Journal of Cosmology and Astro-Particle Physics*, 1, 28
- Serra P., Cooray A., 2008, *Physical Review D*, 77, 107305
- Silverstein E., Tong D., 2004, *Phys. Rev. D.*, 70, 103505
- Smith D. J. B., Dunne L., da Cunha E., Rowlands K., Maddox S. J., et al 2012, *MNRAS*, 427, 703
- Smith D. J. B., Dunne L., Maddox S. J., Eales S., Bonfield D. G., et al. 2011, *MNRAS*, 416, 857
- Starobinskiĭ A. A., 1979, *Soviet Journal of Experimental and Theoretical Physics Letters*, 30, 682
- Tegmark M., Efstathiou G., 1996, *MNRAS*, 281, 1297
- The COre Collaboration Armitage-Caplan C., Avillez M., Barbosa D., Banday A., et al. 2011, (arXiv:1102.2181)
- Toffolatti L., Negrello M., González-Nuevo J., de Zotti G., Silva L., Granato G. L., Argüeso F., 2005, *A&A*, 438, 475
- Tucci M., Martínez-González E., Toffolatti L., González-Nuevo J., De Zotti G., 2004, *MNRAS*, 349, 1267
- Tucci M., Toffolatti L., 2012, *Advances in Astronomy*, Volume 2012, Article ID 624987.
- Tucci M., Toffolatti L., de Zotti G., Martínez-González E., 2011, *A&A*, 533, A57
- Vaillancourt J. E., 2011, in Bastien P., Manset N., Clemens D. P., St-Louis N., eds, Vol. 449 of *Astronomical Society of the Pacific Conference Series*, *Observations of Polarized Dust Emission at Far-infrared through Millimeter Wavelengths*. p. 169
- van Kampen E., Smith D. J. B., Maddox S., Hopkins A. M., Valtchanov I., et al. 2012, *MNRAS*, 426, 3455
- Verde L., Wang L., Heavens A. F., Kamionkowski M., 2000, *MNRAS*, 313, 141
- Viero M. P., Wang L., Zemcov M., Addison G., Amblard A., et al. 2012, (arXiv:1208.5049)
- Wang J., Navarro J. F., Frenk C. S., White S. D. M., Springel V., Jenkins A., Helmi A., Ludlow A., Vogelsberger M., 2011, *MNRAS*, 413, 1373
- Xia J.-Q., Negrello M., Lapi A., De Zotti G., Danese L., Viel M., 2012, *MNRAS*, 422, 1324
- Yadav A. P. S., Komatsu E., Wandelt B. D., 2007, *ApJ*, 664, 680
- Yadav A. P. S., Wandelt B. D., 2010, *Advances in Astronomy*, Volume 2010, Article ID 565248.
- York D. G., Adelman J., Anderson Jr. J. E., Anderson S. F., Annis J., SDSS Collaboration 2000, *AJ*, 120, 1579
- Zhao D. H., Mo H. J., Jing Y. P., Börner G., 2003, *MNRAS*, 339, 12